3-D Strain Imaging Using a Rectilinear 2D Array

Samer I. Awad and Jesse T. Yen
Dept. of Biomedical Engineering, University of Southern California, Los Angeles, USA

***Abstract*—Under mechanical compression, tissue movements are inherently three-dimensional. 2-D strain imaging can suffer from decorrelation noise caused by out-of-plane tissue movement in elevation. With 3-D strain imaging, all tissue movements can be estimated and compensated, hence minimizing out-of-plane decorrelation noise. Promising 3-D strain imaging results have been shown using 1-D arrays with mechanical translation in elevation. However, the relatively large slice thickness and mechanical translation can degrade image quality. Using 2-D arrays, a better elevational resolution can be achieved with elevational focusing. Furthermore, scanning with 2-D arrays is done electronically, which eliminates the need for mechanical translation. In this paper, we present our initial 3-D strain images of gelatin/agar phantoms using a 4cm x 4cm ultrasonic sparse rectilinear 2-D array operating at 5MHz.**

Keywords- strain imaing; sparse 2-D array; 3-D imaging; sum absolute differences (SAD);

I. INTRODUCTION

Since its start in 1991 by Ophir et al. [1], there has been significant progress in strain imaging, a technique used for visualizing the mechanical stiffness of biological tissue. It is based on applying static or dynamic mechanical compression to a tissue sample, collecting pre- and post-compression radio frequency (RF) data and using signal processing methods to evaluate strain by calculating displacements and applying a gradient operation to estimate strain [1,2].

To date, strain imaging has largely been done in two dimensions [2,3]. Since tissue movement is inherently three-dimensional, these images can suffer from decorrelation noise caused by out-of-plane tissue movement in elevation if the tissue is not physically confined [2,4]. Some techniques involved 1-D and 2-D companding in which post-compression RF data are compressed or expanded to improve coherence with pre-compression data and minimize decorrelation errors caused by azimuthal and elevational tissue movement [2]. 3-D companding results were also reported showing more improvement in the strain image quality since it accounts for out-of-plane tissue movement [4].

3-D strain imaging has the potential to capture virtually all tissue movement, hence minimizing decorrelation noise. It can also provide additional data about the tumor that could help in characterizing the tumor as benign or malignant such as the shape and volume of the tumor [5].

Some 3-D ultrasound systems use a 1-D array with mechanical translation in the elevational direction using motorized or freehand methods to acquire multiple B-scans followed by reconstruction to create the 3-D image [6]. A 1-D linear sequential array has transducer elements along the azimuthal direction only. The acoustic lens of a 1-D array focuses the beam at a single, predetermined depth. The beam is well focused in elevation at this depth, but diverges at depths away from the focus degrading image quality due to the increase in slice thickness. Consequently, dynamic focusing – using 1-D arrays-of can be done in azimuth only. 2-D arrays, on the other hand, have equal dynamic focusing capability in both lateral directions, which make them capable of producing a thinner slice thickness since dynamic elevation focusing is possible. Overall, 2-D arrays have advantages of higher speed, more reliability, and better elevational resolution through electronic focusing.

The acoustic lens of a 1-D array focuses the beam at a single, predetermined depth. The beam is well focused in elevation at this depth, but diverges at depths away from the focus degrading image quality due to the increase in slice thickness. 2-D arrays, on the other hand, have equal focusing capability in both lateral directions (Figure 1b), which make them capable of producing a thinner slice thickness since dynamic elevation focusing is possible. Overall, 2-D arrays have advantages of higher speed, more reliability, and better elevational resolution through electronic focusing.

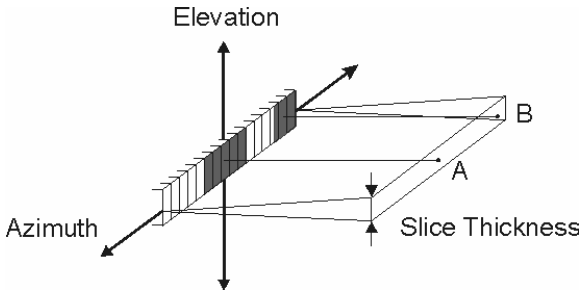

Fig. 1a

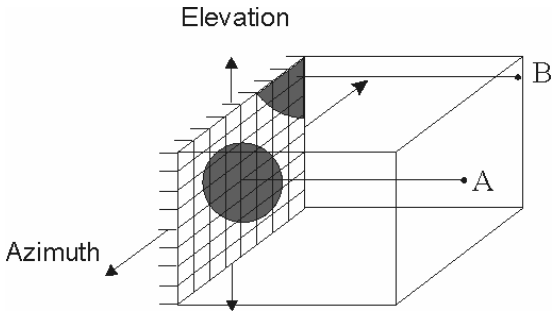

Fig. 1b

Figure 1. 1-D linear array and 2-D rectilinear array and their fields of view

II. METHODS

A. System Description

The experimental setup used here consists of a sparse 2-D array, 4:1 receive mode multiplexers and Ultrasonix (Richmond, BC, Canada) Sonix RP ultrasound system. The prototype sparse 2-D array has a 40 x 40 mm aperture, 5 MHz center frequency, 45% -6 dB fractional bandwidth, 1024 receivers, 169 transmitters and scans a 40 x 40 x 60 mm 3-D rectilinear volume [7]. The array consists of 13 x 13 = 169 transmit elements, each having dimensions of 2.4 x 2.4 mm. Four receive elements with dimensions of 0.6 x 0.6 mm are embedded in a staggered pattern inside each of the transmit pistons (Figure 2).

The Ultrasonix Sonix RP ultrasound system with research capability has a 40 MHz sampling frequency, 128 transmit channels and 32 receive channels. Using Texo, a C++ program provided by Ultrasonix, this system allows the user to acquire raw radio frequency (RF) data and it gives the user control over transmit aperture size, transmitted power, transmitted frequency, receive aperture size, receive gain and acquisition length.

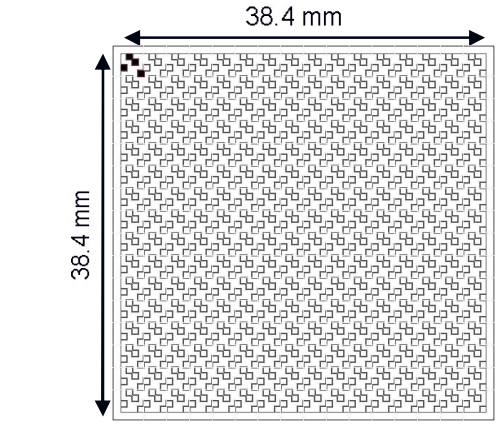

a. Schematic of the entire array

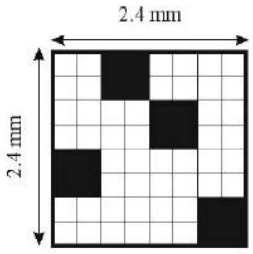

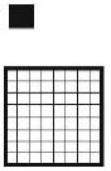

b. Schematic of a single cell with 0.6 × 0.6 mm receive elements and surrounding transmitters.

Figure 2. Sparse 2-D array

To acquire the RF data from the 1024 receive elements, an additional multiplexing circuit was used to interface the receive elements to the 128 channels of the system. In previous work we designed a 4:1 multiplexer board which uses 32 MAX4052/A dual 4:1 multiplexers (Maxim Integrated Products, Sunnyvale, CA, USA) [7].

We used the parallel port of the Ultrasonix system along with C++ commands embedded in Texo to control the addressing of the multiplexer boards. All RF signals were acquired 32 times and averaged.

B. Phantom fabrication

70 x 70 x 70 mm gel based phantoms with stiff agar inclusions were used to test 3-D strain imaging system. The following recipes were used: Background material: 400 g DI water, 36.79 g N-propanol, 0.238 g Formaldehyde, 24.02 g Gelatin (275 Bloom) and 3.89 g Graphite. Inclusion material: 50 g DI water, 4.6 g N-propanol, 0.103 g Formaldehyde, 1.1 g Agar and 1.15 g Graphite [8].

C. Data collection and signal processing

3-D beamforming: Using a synthetic aperture approach in 3-D beamforming, one transmit element was excited and signals from all 1024 receive elements were acquired. This process was repeated for the 169 transmit elements of the array. Off-line 3-D beamforming was applied to the RF element data using Matlab (Mathworks Inc., Natick, MA) to create our pre- and post-compression 3-D RF echo fields. Azimuthal and elevational receive dynamic focusing every 1 mm was used along with an expanding aperture to keep the F number at 2. The resulting B-mode image was 38.4 x 38.4 x 41.6 mm with 129 x 129 = 16,641 RF lines and 0.3 mm line spacing. The RF data were band pass filtered in Matlab.

3-D strain imaging: The first step in 3-D strain imaging is to estimate displacements between the pre- and post-compression RF data which are linearly proportional to axial tissue displacement. Since 3-D displacement estimation involves heavy processing of big data sizes, a fast method was needed. The sum of absolute differences (SAD) algorithm was used since it provides similar performance to cross correlation but with 8 times fewer arithmetic operations [2]. This method involves taking a 3-D kernel of pre-compression data and applying a 3-D search for the best matching kernel of the same size in the post-compression data. The output of this search is a 3-D matrix of coefficients. The minimum value of this matrix corresponds to the best match and its location in 3-D corresponds to the estimated tissue displacement. In our approach we have done displacement estimation in two steps. In the first step, coarser displacements were calculated with non-overlapping kernels with the size of 0.6 mm axially and 1 mm in azimuth and elevation and 1 mm axial and 1 mm lateral separation between kernels. A search window size of 1 x 1.1 x 1.1 mm (54x7x7 samples) was chosen by visual inspection. Sometimes, a false minimum value in the coefficients matrix becomes smaller than the true minimum. To minimize the number of false minima in this step, median filtering was used [9]. In the second step, finer time delays were calculated using overlapping kernels with a size of 0.6 mm axially and 1 mm in both lateral directions and 0.1 mm axial and 0.3 mm lateral

separation between kernels[2]. This SAD coefficients matrix was spline interpolated by a factor of 5 axially. The number of false minima was minimized in this step by using the coarse time delays as the center for the search window with the size of 0.1 x 1.1 x 1.1 mm (7x7x7 samples) [2,3]. The resulting axial displacements were then averaged over a 1.7 mm window [10]. Axial strain was estimated by calculating the gradient of two adjacent values of the averaged displacements in the axial direction.

III. Results

3-D pre-compression and post-compression RF data sets of the 70 x 70 x 70 mm gel based phantoms with 12 mm, 9 mm and 6 mm diameter stiff agar cylindrical and spherical inclusions were obtained using the sparse 2-D array. The phantoms were compressed using a 125 x 125 mm aluminum plate with a 1.5% axial compression. Figure 3 presents the 3-D axial strain image (generated using 3-D beamforming and 3-D displacement estimation) of the cylindrical inclusion phantoms in a collage of slices in 3 orthogonal planes: azimuth, elevation and axial.

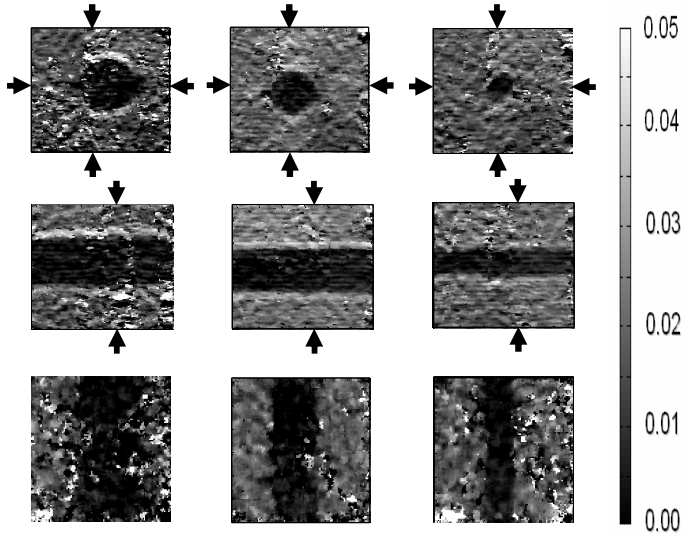

Figure 3. Collage of slices in azimuthal, elevational and axial slices of the 3-D axial strain image of the 12 mm, 9 mm and 6 mm (left to right) cylindrical inclusion phantoms generated using 3-D beamforming and 3-D displacement estimation. Top row: azimuthal slices. The arrows indicate where the elevational and axial slices were taken. Middle row: elevational slices. The arrows indicate where the azimuthal slices were taken. Bottom row: Axial slices. The size of the images is 27 mm axially and 30 mm in azimuth and in elevation. The transducer is located on top of the azimuthal and elevational slices and parallel to the axial slices.

In Figure 4, 3 perpendicular slices of the 9 mm cylindrical inclusion phantom 3-D axial strain image (generated using 3-D beamforming and 3-D displacement estimation) are shown.

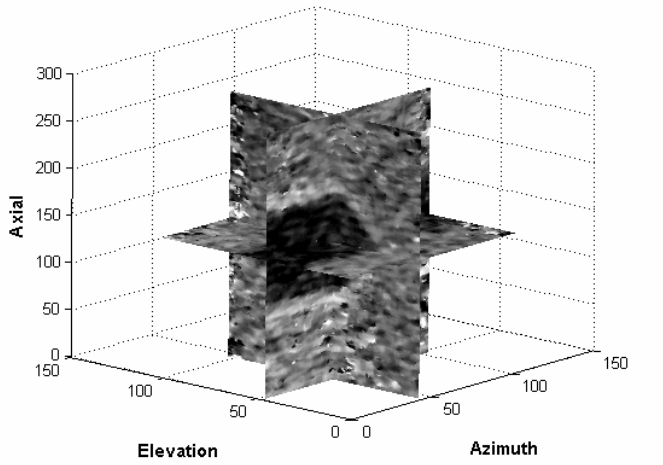

Figure 4. Perpendicular slices of the 9 mm cylindrical inclusion phantom 3-D strain image generated using 3-D beamforming and 3-D displacement estimation. The transducer is located at the bottom of the image.

Figure 5 is another collage of elevational, azimuthal and axial slices of the 3-D axial strain images (generated using 3-D beamforming and 3-D displacement estimation) of the spherical inclusion phantoms.

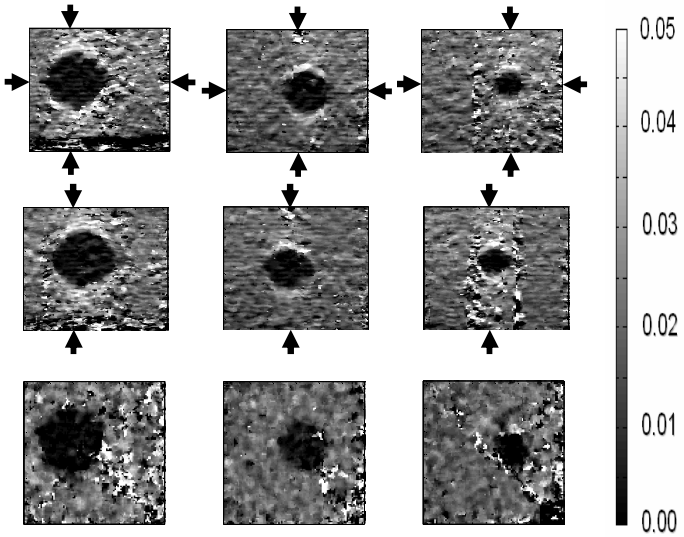

Figure 5. Collage of slices in azimuthal, elevational and axial slices of the 3-D axial strain image of the 12 mm, 9 mm and 6 mm (left to right) spherical inclusion phantoms generated using 3-D beamforming and 3-D displacement estimation. Top row: azimuthal slices. The arrows indicate where the elevational and axial slices were taken. Middle row: elevational slices. The arrows indicate where the azimuthal slices were taken. Bottom row: Axial slices. The size of the images is 27 mm axially and 30 mm in azimuth and in elevation. The transducer is located on top of the azimuthal and elevational slices and parallel to the axial slices.

Figure 6 shows 3 perpendicular slices of the 3-D axial strain image (generated using 3-D beamforming and 3-D displacement estimation) of the 9 mm spherical inclusion phantom. The size of the images in Figures 3 to 6 is 30 mm in azimuth and elevation and 27 mm axially.

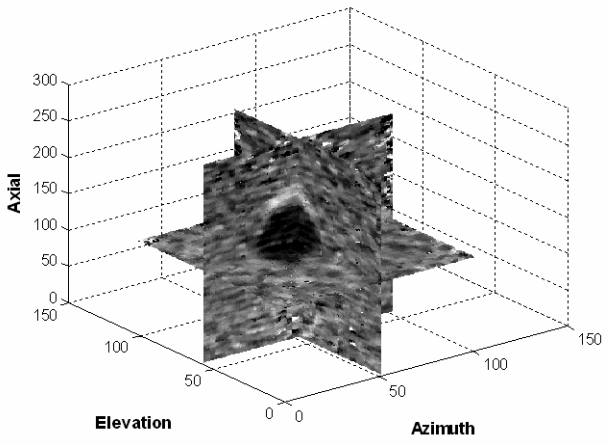

Figure 6. Perpendicular slices of the 9 mm spherical inclusion phantom 3-D axial strain image generated using 3-D beamforming and 3-D displacement estimation. The transducer is located at the bottom of the image.

Performance was evaluated using contrast to noise ratio (CNR) [2]:

$$CNR = \sqrt{\frac{2(\bar{s}_t - \bar{s}_b)^2}{var\, s_t + var\, s_b}} \quad \text{(Eq. 1)}$$

In Equation 1, $\bar{s}$ and var s denote mean and variance, respectively. The subscripts t and b represent the target and background, respectively. CNR values were estimated using 3-D kernels chosen from inside the inclusion (s_t) and from the background (s_b).

A CNR kernel size of 26x13x9=3042 voxels or 2.5x3.9x2.7=26.3 mm^3 (axially, in elevation and in azimuth respectively) was used in all cases. The CNR values for the 12, 9 and 6 mm cylindrical inclusion phantoms were 2.35, 3.12 and 2.79 respectively. The CNR values for the 12, 9 and 6 mm spherical inclusion phantoms were 2.33, 3.39 and 3.32 respectively.

IV. Conclusions and Future Work

Using offline synthetic aperture 3-D beamforming and 3-D time delay estimation, we have presented 3-D strain images using our sparse rectilinear 2-D array.

In future work, different algorithms to improve strain images quality will be investigated including 3-D spatial compounding and 3-D companding [4]. Furthermore, in vitro animal experiment will be conducted to test the 3-D ultrasonic strain IMAGING SYSTEM MORE RIGOROUSLY [11].

ACKNOWLEDGMENT

Special thanks to Michael Insana, Jean Tsou, and Mallika Keralapura for help with strain imaging algorithms.

References

[1] [Ophir, J., Elastography, a quantitative method for imaging the elasticity of biological tissue. ultrason. imag., 1991. 13: p. 111–134

[2] Chaturvedi, P., M.F. Insana, and T.J. Hall, 2-D companding for noise reduction in strain imaging. IEEE Trans. Ultrason., Ferroelect., Freq. Contr., 1998. 45(1): p. 179-191

[3] Zahiri-Azar, R. and S.E. Salcudean, Motion estimation in ultrasound images using time domain cross correlation with prior estimates. IEEE Trans. on Biomedical Eng., 2006. 53(10).

[4] Insana, M.F., et al., 3-D Companding using linear arrays for improved strain imaging. 1997 IEEE Ultrasonics Symposium, 1997 Proceedings, 1997. 2: p. 1435-1438

[5] Sahiner, B., et al., Computerized characterization of breast masses on three-dimensional ultrasound volumes. Medical Physics, 2003. 31(4): p. 744-754

[6] Fenster, A. and D.B. Downey, 3-D ultrasound imaging: a review. IEEE Engineering in Medicine and Biology Magazine, 1996. 15(6): p. 41-51.

[7] Yen, J.T. and S.W. Smith, Real-time rectilinear volumetric imaging using receive mode multiplexing. IEEE Trans. Ultrason., Ferroelect., Freq. Contr., 2004. 51: p. 216-226.

[8] Hall, T.J., et al., Phantom materials for elastography. IEEE Trans. Ultrason., Ferroelect., Freq. Contr., 1997. 44(6): p. 1355-1365.

[9] Righetti, R., J. Ophir, and P. Ktonas, Axial resolution in elastography. Ultrasound Med. Biol., 2002. 28(1): p. 101-113.

[10] Pellot-Barakat, C., M.F. Insana, and A. Herment, Ultrasound elastography based on multiscale estimations of regularized displacement fields. IEEE Trans on Medical Imaging, 2004. 23(2).

[11] Bilgen, M., et al., Elastography imaging of small animal oncology models: a feasibility study. Ultrasound in Medicine and Biology 2003. 29(9): p. 1291-1296.